JOURNAL OF PROPULSION AND POWER
Vol. 24, No. 2, March–April 2008

Experimental Study of Chin Intakes for Airbreathing Missiles with High Agility

Dirk Herrmann,* Klaus Triesch,† and Ali Gülhan‡
Institute of Aerodynamics and Flow Technology German Aerospace Center, 51147 Cologne, Germany

DOI: 10.2514/1.29672

The performance of three chin intakes for airbreathing missiles with high agility has been investigated in a large maneuver range at supersonic speed. This experimental study is based on former studies on axially symmetrical intake models, in which losses of pressure recovery and mass flow were discovered at angles of attack greater than 18 deg. To understand these effects in more detail, chin intakes have been analyzed at a design Mach number of 3.0 at angles of attack ranging from −30 to 30 deg and at angles of sideslip ranging from −30 to 30 deg in the Trisonic Wind Tunnel. The results clearly show that boundary-layer flow, vortices, and flow separation are responsible for the losses of pressure recovery and mass flow. The subsequently added boundary-layer bleed permits a better pressure recovery and a delay of the intake buzzing.

Nomenclature

A	=	cross-sectional area
l	=	reference length
M	=	Mach number
$\dot{m}$	=	mass flow rate
p	=	pressure
R	=	specific gas constant
Re	=	Reynolds number
T	=	temperature
v	=	flow velocity
x, y	=	Cartesian coordinates
x, φ	=	polar coordinates
α	=	angle of attack
β	=	angle of sideslip
Δ	=	difference
δ_{cone}	=	angle of the cone
δ_{cowl}	=	angle of the cowl
Θ_1	=	first cone shock relating to the x axis
Θ_2	=	second cone shock relating to the x axis
κ	=	heat capacity ratio
γ_E	=	opening angle of intake entrance
μ	=	viscosity
ρ	=	density

Subscripts

D	=	design (shock on lip)
lip	=	position at the cowl's lip
st	=	static condition
t	=	total condition
throat	=	position at the throat
0	=	freestream condition
1, 2	=	positions after each cone shock
3	=	position of the measurement pipe cross section where pressure measurements are located
4	=	position of the critical throttle cross section
I–IV	=	positions on the x axis

Received 9 January 2007; revision received 3 December 2007; accepted for publication 4 December 2007.

*Research Scientist, Wind Tunnel Department, Linder Höhe; dirk.herrmann@dlr.de.
†Retired Research Scientist, Wind Tunnel Department, Linder Höhe.
‡Head of Department, Wind Tunnel Department, Linder Höhe; ali.guelhan@dlr.de. Member AIAA.

I. Introduction

AIRBREATHING propulsion is used on airplanes and supersonic missiles. The latter type is a ramjet, which has no rotating parts and needs to reach a certain speed and altitude to self-start. To keep the combustion stable, the intake must provide the engine with the right air mass flow and the required pressure recovery. It is therefore important to investigate the ramjet's performance for flight conditions at high angles of attack and sideslip [1,2].

Several studies have been carried out on the performance of axially symmetrical intakes, including unstart criteria and intake buzzing [3]. Buzzing must be prevented [4] to ensure the functionality of the ramjet and prevent destruction of the engine structure. Another means of improving performance is the use of boundary-layer bleed [5–7], which is of great importance.

Based on the results and open issues of these studies, the purpose of this study is to clarify the influence of the main flow parameters on the intake behavior and to specify the ramjet's performance for a flexible maneuver range. This flexible maneuver range refers to the phase in which the missile approaches the target at large angles. In this phase, the airbreathing engine must be operational.

In the run up to this study, axially symmetrical intakes were tested [8]. The tests reveal different shock and vortex systems, which enter and affect the intake together. They are responsible for losses of mass flow and pressure recovery at angles of attack $\alpha \geq 18$ deg. As a consequence and to analyze these effects separately, a segment of the previously axially symmetrical intake entrance is used for further studies. This segment is positioned like a chin under the main missile body.

This paper contains the experimental techniques and results for the chin intakes at a freestream Mach number of $M_0 = 3.0$ with an angles of attack ranging from -30 deg $\leq \alpha \leq 30$ deg and sideslip ranging from -30 deg $\leq \beta \leq 30$ deg. This study shows, among other things, the itemized effects of windward and leeward flow at small and large angles of attack and sideslip and the comparison of the chin intakes with each other and with the axially symmetrical intake as well.

In Sec. II, the wind tunnel and the intake models are described. Experiments with different chin intakes are carried out with and without boundary-layer bleed. Furthermore, the intake characteristics, that is, the pressure recovery and mass flow rate, are analyzed with schlieren images, oil flow visualization, and pressure

measurement. Finally, the main results of this study are summarized and some conclusions and suggestions for future studies are given.

II. Experimental Setup

A. Trisonic Wind Tunnel, Cologne

The experiments were conducted in the Trisonic Wind Tunnel (TMK) [9] of the German Aerospace Center (DLR) in Cologne. The TMK is a blowdown wind tunnel with a cross section of 0.6×0.6 m. It is equipped with a flexible nozzle, which can be adjusted while testing. A test duration of 60 sec is possible, depending on Mach and Reynolds numbers. Its standard Mach number range is $1.25 < M_0 < 4.5$. Mach numbers up to 5.7 can be achieved with the aid of a storage heater and an ejector. The ejector facilitates a Reynolds number variation by a factor of up to 7. For Mach numbers of $0.5 < M_0 < 1.2$, a transonic test section with perforated walls is available.

B. Models and Flow Conditions

The intake models with mixed compression were designed in Herrmann and Triesch [8] with the characteristic-method program based on Anderson [10], which has in-house modifications. In Herrmann and Triesch [8], two axially symmetrical intakes were tested. For the present study, the intake (HaFK-2) with the larger pressure recovery was chosen for the construction of the chin intakes.

These intakes are designed for a freestream Mach number of $M_D = 3.0$ (shock on lip) and have a self-start Mach number of $M_0 = 2.2$. The compression limit [11,28] at $M_0 = 3.0$ is 18.6% and 8.9% at $M_0 = 2.2$; because the intakes' internal compression is 8.8%, the self-start is possible. Using Eq. (1) in accordance with [12], the compression limit is calculated with the entrance plane A_{lip} at the cowl's lip, its Mach number M_{lip}, and the throat's plane A_{throat}:

$$\frac{A_{\text{lip}}}{A_{\text{throat}}} = \frac{1}{M_{\text{lip}}} \cdot \left[\frac{(\kappa+1)\cdot M_{\text{lip}}^2}{(\kappa-1)\cdot M_{\text{lip}}^2+2}\right]^{\frac{\kappa}{\kappa-1}} \cdot \left[\frac{\kappa+1}{2\cdot\kappa\cdot M_{\text{lip}}^2-(\kappa-1)}\right]^{\frac{\kappa}{\kappa-1}} \cdot \left[\frac{2+(\kappa-1)\cdot M_{\text{lip}}^2}{\kappa+1}\right]^{\frac{\kappa+1}{2(\kappa-1)}} \tag{1}$$

The geometric contour is given in Table 1. The chin intakes only differ in the size of the entrance segment, which are presented with the other parts of the model in Fig. 1.

The segments have an entrance opening angle of $\gamma_E \approx 50$, 70, and 90 deg. They can be separately mounted under the main body. The chin intake uses the cone of the main body ($\delta_{\text{cone},1}$) for the first external compression. The cone ($\delta_{\text{cone},2}$) on the segment element is used for the second external compression. One of these segment elements can be bolted to the manifold, which is attached to the hollow main body. The assembled model mounted in the TMK can be seen in Fig. 2.

After the experiments (without boundary-layer bleed) had been accomplished, the intake model was modified for tests with boundary-layer bleed. A 3 mm wide slot was inserted at the throat in every intake segment (Fig. 3). This slot allows a certain amount of boundary layer and mass flow to leave the intake through the holes in the main body.

The three airbreathing intakes are tested between angles of attack of −30 and 30 deg and (by exploiting the symmetry) between angles of sideslip of 0 and 30 deg at increments of 3 deg without and with boundary-layer bleed (see Table 2). The flow condition is given in Table 3 and its percentage error of measurement is given in Table 4.

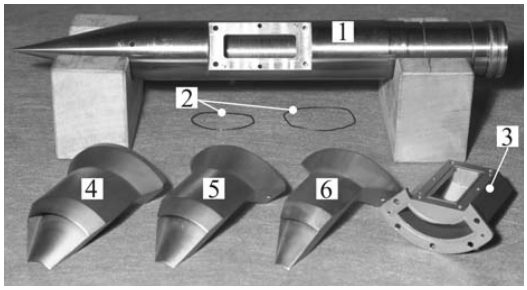

1	Main body	4	90-deg segment
2	Gasket	5	70-deg segment
3	Manifold	6	50-deg segment

Fig. 1 Disassembled intake model.

Fig. 2 Assembled 90-deg intake model at $\alpha = 30$ deg.

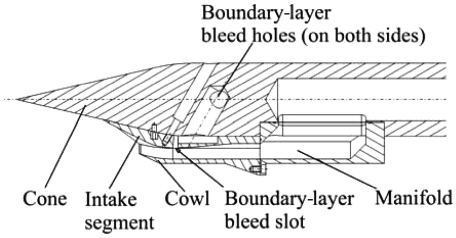

Fig. 3 Sketch of the boundary-layer bleed system.

C. Measurement Technique

To investigate the intake's performance, mass flow and pressure recovery have to be measured and illustrated. For this purpose, a measurement configuration is required, which is shown in Fig. 4.

The measurement configuration consists of the intake, which is mounted to the front of the measurement pipe, and the throttle, which is connected to the downstream end. The throttle was calibrated using a calibration standard based on orifice technology [12,13]. The mass flow rate through the throttle is determined with the sonic flow

Table 1 Geometry of chin-intake models

Model	γ_E, deg	$\delta_{\text{cone},1}$, deg	$\delta_{\text{cone},2}$, deg	δ_{cowl}, deg	Inside compression, %
50-deg intake	49.1	13.0	27.0	17.0	8.8
70-deg intake	69.2	13.0	27.0	17.0	8.8
90-deg intake	88.4	13.0	27.0	17.0	8.8

Table 2 Test conditions

Model	α range, deg	β range, deg	Boundary-layer bleed
50-deg intake	$-30\cdots30$	0	Without/with
50-deg intake	0	$0\cdots30$	Without/with
70-deg intake	$-30\cdots30$	0	Without/with
70-deg intake	0	$0\cdots30$	Without/with
90-deg intake	$-30\cdots30$	0	Without/with
90-deg intake	0	$0\cdots30$	Without/with

Table 3 Freestream conditions

M_0	T_{t0}, K	$p_{t0}, \cdot 10^5$ Pa	$Re, \cdot 10^7$ m^{-1}
3.0	280	5.8	4.8

Table 4 Measurement inaccuracies

$\Delta M_0/M_0$, %	$\Delta T_{t0}/T_{t0}$, %	$\Delta p_{t0}/p_{t0}$, %	$\Delta Re/Re$, %
0.50	0.75	0.02	0.04

method. Another function of the throttle is to simulate the pressure in the combustion chamber. This pressure is varied by moving the throttle, that is, changing the critical throttle cross section. The throttle is controlled by a hydraulic system. Upstream of the throttle, the measurement pipe is fitted, with pressure taps positioned at its end to measure the static pressure p_{st3}. This pressure value combined with the total temperature data and critical throttle cross-sectional geometry are used for the calculation of the intake performance data. The exact position of the throttle is therefore required. It is determined with an integrated potentiometer, whose output signal defines the variable throttle cross-sectional area A_4. For further calculations, the continuity equation $\dot{m}_3 = \dot{m}_4$ is used with the following boundary conditions: the Mach number at the throttle cross section 4 is $M_4 = 1$, the isentropic flow of $T_{t3} = T_{t4}$ is assumed, and the pressure loss is negligible, that is, $p_{t3} = p_{t4}$. This yields

$$\frac{A_3}{A_4} = \frac{1}{M_3} \cdot \left(\frac{1 + \frac{\kappa-1}{2} \cdot M_3^2}{\frac{\kappa+1}{2}} \right)^{\frac{\kappa+1}{2(\kappa-1)}} \tag{2}$$

Using Eq. (2), M_3, which is needed for the mass flow ratio, can be calculated iteratively

$$\frac{\dot{m}_3}{\dot{m}_0} = \frac{1}{\dot{m}_0} \cdot \frac{p_{t3}}{\sqrt{R \cdot T_{t0}}} \cdot A_3 \cdot M_3 \cdot \sqrt{\kappa} \cdot \left(1 + \frac{\kappa - 1}{2} \cdot M_3^2 \right)^{-\left(\frac{\kappa+1}{2(\kappa-1)}\right)} \tag{3}$$

where p_{t3} is

$$p_{t3} = p_{st3} \cdot \left(1 + \frac{\kappa - 1}{2} \cdot M_3^2 \right) \tag{4}$$

and $\dot{m}_3 = \rho_3 \cdot v_3 \cdot A_3$ was extended with the undisturbed mass flow $\dot{m}_0$ at $\alpha = 0$ deg. $\dot{m}_0$ is calculated, for instance, with the static pressure p_{st0} and static temperature T_{st0}

$$\dot{m}_0 = \frac{p_{st0}}{\sqrt{R \cdot T_{st0}}} \cdot A_0 \cdot M_0 \cdot \sqrt{\kappa} \tag{5}$$

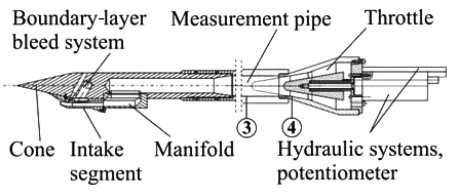

Fig. 4 Measurement configuration.

Table 5 Measurement inaccuracies

$\Delta p_{st3}/p_{st3}$, %	$\Delta A_3/A_3$, %	$\Delta(p_{t3}/p_{t0})/(p_{t3}/p_{t0})$, %	$\Delta(\dot{m}_3/\dot{m}_0)/(\dot{m}_3/\dot{m}_0)$, %
0.02	0.03	0.04	1.19

with the projected intake plane A_0 at right angles to the incident flow at M_0. Pressure recovery is expressed as

$$\frac{p_{t3}}{p_{t0}} = \frac{p_{st3}}{p_{t0}} \cdot \left[1 + \frac{(\kappa - 1)}{2} \cdot M_3^2 \right]^{\frac{\kappa}{\kappa-1}} \tag{6}$$

The major measurement inaccuracies of the aforementioned performance data are presented in Table 5.

Both ratios (mass flow ratio and pressure recovery) are plotted on the intake characteristic diagram, as shown in Fig. 5.

The intake characteristic diagram shows the test procedure. At the beginning, the maximal mass flow ratio with a low pressure recovery is detected while the throttle is open. During the test, the throttle closes continuously (represented by the arrow in Fig. 5). This event appears as a vertical line with a constant mass flow rate and rising pressure recovery (supercritical condition). The pressure rises while the throttle is closing, during which the normal shock moves upstream. When the normal shock reaches the intake's throat, the maximal pressure recovery (critical condition) is achieved. The theoretical maximal pressure recovery for a three-shock system with two oblique shocks and a normal shock at $M_0 = 3.0$ is 75% [14–16], in which each oblique shock is of equal strength [15]. With an increase in pressure, the shock leaves the intake and takes the form of a detached shock (subcritical condition) upstream. This shock in front of the intake's entrance causes mass flow loss, because only a part of the incident flow enters the intake and the other part is spillage. This detached shock can be stable at first. With further throttling, the shock grows unstable until it finally jumps in and out of the intake. This unstable condition with pressure fluctuations is known as buzzing [17]. The buzzing is detected with an rms meter and is depicted by vertical lines in the subcritical region, whereas the buzzing value is normalized with p_{t0}. If this value becomes too large, the abort criterion is reached and the throttle opens at once. This response is necessary, because the pressure fluctuations can cause strong structural loads and can damage the model.

For investigations of the flow effects, schlieren images [18] and oil visualization are used. Further static pressure is measured on the cone. An additional cone model with the same geometry as the front part of the main body was therefore built (Fig. 6). The cone's angle is 26 deg and the cone-shaped shell is equipped with 16 pressure taps. The pressure taps are arranged in five rows, aligned in the x axis direction and rotated in 45 deg steps ($\varphi = 0$ deg is the center of the leeward side). Inside the cone are thin tubes, which lead from the pressure taps to an electronic-pressure scanner (64 psi).

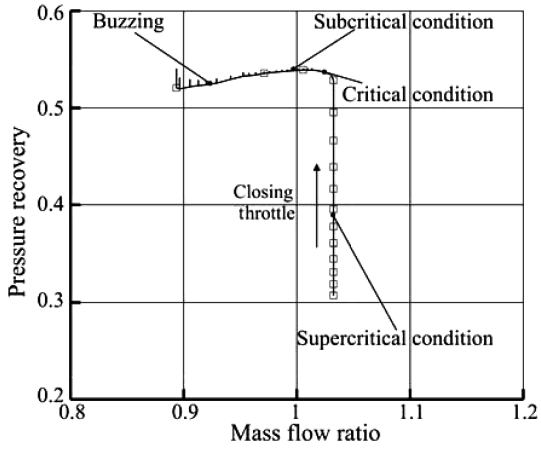

Fig. 5 Example of the intake characteristic diagram.

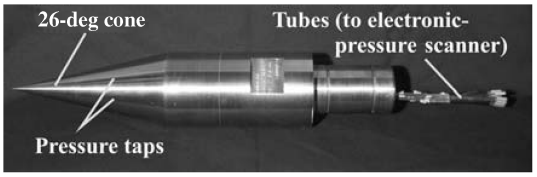

Fig. 6 Cone model with static pressure taps.

III. Experimental Results

A. Effects of Boundary-Layer Bleed

Tests were first conducted without boundary-layer bleed. After completion of these tests had been accomplished, boundary-layer bleed was implemented to improve the intake's performance and to compare the intake's results. Figure 7 shows the characteristic diagram of the 50-deg intake without boundary-layer bleed with positive angles of attack (at $\alpha = 9$ deg, only the supercritical region is measured) and Fig. 8 with negative angles of attack at $M_0 = 3.0$.

At $\alpha = 0$ deg, the characteristic of the 50-deg intake reveals a pressure recovery of 52% (the 70- and the 90-deg intake reveal a pressure recovery of 52 and 51%, respectively). At positive angles of attack up to $\alpha = 9$ deg, the maximum pressure recovery is almost constant and the mass flow ratio increases to more than 1.0 (Fig. 7). Because the reference mass flow rate $\dot{m}_0$ is defined for the freestream gas parameters and the intake entrance cross-sectional area is at $\alpha = 0$ deg [see Eq. (5)], a higher value can be achieved. The reason will be explained in greater detail in the next chapter. At angles of attack above 9 deg, the mass flow ratio and the pressure recovery decrease with the increasing angle of attack. At negative angles of attack, the characteristics develop differently (Fig. 8). In contrast to the positive angle of attack, mass flow and pressure recovery continuously decrease with an increase in the negative angle; this will also be explained in greater detail in Sec. III.B.

In the supercritical operation, a mass flow ratio of 1.0 is expected at an angle of attack of $\alpha = 0$ deg, but here it is not the case. The main reasons are minor imperfections in the model fabrication, which result in minor spillage caused by the shock displacement, and boundary-layer effects, which are not fully accounted for by the design program [10].

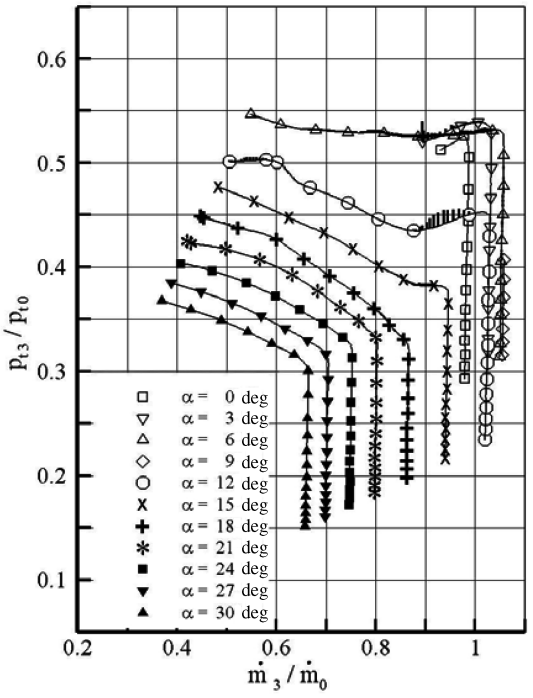

Fig. 7 Characteristic diagram of the 50-deg intake, positive α, $M_0 = 3.0$.

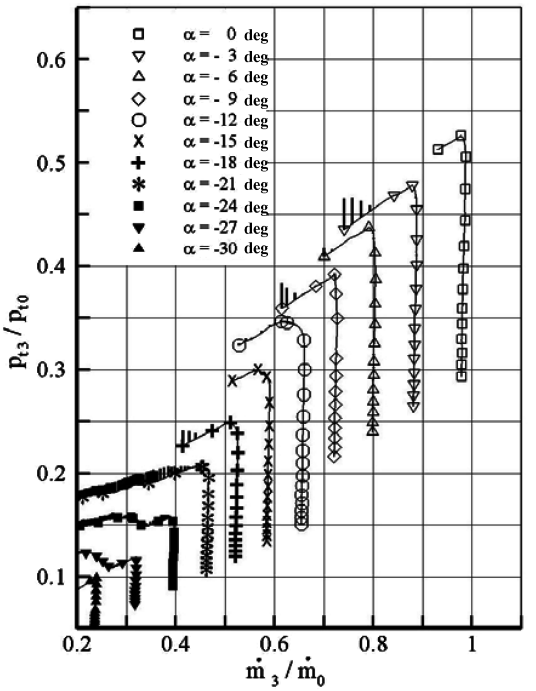

Fig. 8 Characteristic diagram of the 50-deg intake, negative α, $M_0 = 3.0$.

To compare the supercritical mass flow ratios of all three chin intakes including the axially symmetrical intake (360-deg intake), the mass flow ratio is normalized with its mass flow ratio of the angle at 0 deg

$$\frac{\text{mass flow ratio of } \alpha}{\text{mass flow ratio of } \alpha = 0 \text{ deg}} = \frac{\frac{\dot{m}_3}{\dot{m}_0}}{\frac{\dot{m}_{3,\alpha=0 \text{ deg}}}{\dot{m}_0}} = \frac{\dot{m}_3}{\dot{m}_{3,\alpha=0 \text{ deg}}} \tag{7}$$

and the results are shown in Fig. 9.

A comparison of the axially symmetrical intake with the chin intakes reveals clear differences in the development of the mass flow ratio in relation to the angle of attack. It is therefore obvious that the intermixing windward and leeward side effects of the axially symmetrical intake result in a completely different characteristic. In contrast to the axially symmetrical intake's characteristic, the chin intake's characteristics can be split into three regions. Two regions are on the windward side with positive angles of attack, where at smaller angles a rise in mass flow and at larger angles losses of mass flow are observed. The third region is on the leeward side with negative angles of attack and with a constant decrease in mass flow.

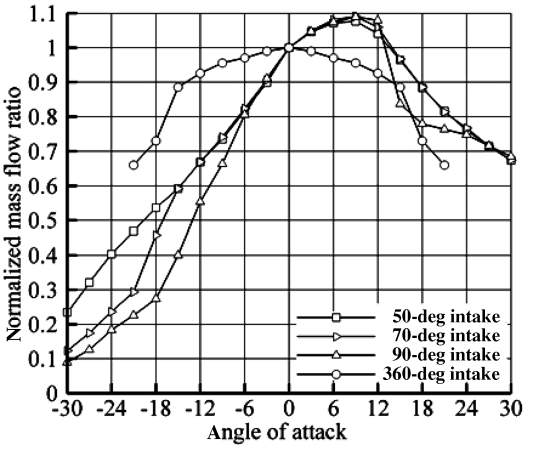

Fig. 9 Normalized mass flow ratios of all intakes at $M_0 = 3.0$, α range, without boundary-layer bleed.

Also clearly visible is the development of the curves, particularly of the 90-deg intake (e.g., an early added 13.5% mass flow loss at around $\alpha = -6$ deg). These effects become more intense with an increase in the opening angle of the intake's entrance from the 50- to the 90-deg intake.

To improve the intake's performance, a boundary-layer bleed is implemented in the intake's throat region. The tests' results with boundary-layer bleed are described below. The application of boundary-layer bleed causes an additive loss in mass flow of about 1–2% at $\alpha = 0$ deg. There are also greater pressure recovery and delayed buzzing. For the 50-deg intake, a larger pressure recovery, surprisingly, is not observed, but for the 70- and the 90-deg intake, a pressure recovery increase of 10.5 and 10.0%, respectively, are detected with $\alpha = 0$ deg. The 90-deg intake is selected to present the mentioned differences due to boundary-layer bleed in Fig. 10. Furthermore, Fig. 10 also shows another improvement due to boundary-layer bleed. Compared with the large mass flow loss of 23.4% in the characteristic diagram without boundary-layer bleed between 12 and 15 deg (Fig. 10a, boundary-layer bleed has a positive effect on performance. The mass flow loss is now significantly lower and reaches 19.7% with an increase in the angle of attack from 15 to 18 deg (Fig. 10b, that is, an improvement in performance of $\Delta\alpha = +3$ deg is observed, combined with lower mass flow loss.

The influence of the boundary-layer bleed on the mass flow rate $\dot{m}_3/\dot{m}_0$ in relation to the angle of attack for the 90-deg intake is summarized in Fig. 11. Between the angles of -3 and $+12$ deg, there is a mass flow decrease of a few percent due to boundary-layer bleed. Particularly conspicuous are the regions between -18 deg $\leq \alpha \leq -6$ deg and 12 deg $\leq \alpha \leq 18$ deg, where the mass flow ratio with boundary-layer bleed is higher than without boundary-layer bleed. Comparing this performance to the 50-deg intake in Fig. 11, no boundary-layer bleed effects are present at -30 deg $\leq \alpha \leq 9$ deg, which is a possible explanation for the aforementioned lack of increase in pressure recovery. Moreover, the mass flow loss ($\alpha > 9$ deg) due to boundary-layer bleed is evident, and the curves with boundary-layer bleed have no distinct regions with higher mass flow ratios. However, the weakened windward side effect with boundary-layer bleed will be explained in Sec. III.B, as well as the fact that the leeward side effects, for example, in connection with the boundary-layer bleed of the 50-deg intake, have no effect on performance at negative angles of attack.

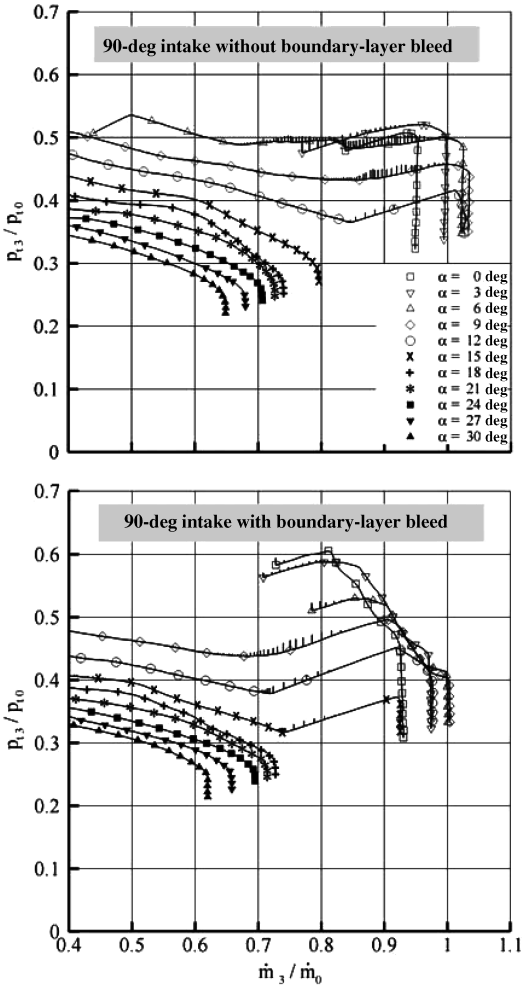

Fig. 10 90-deg intakes at $M_0 = 3.0$: a) without boundary-layer bleed, and b) with boundary-layer bleed.

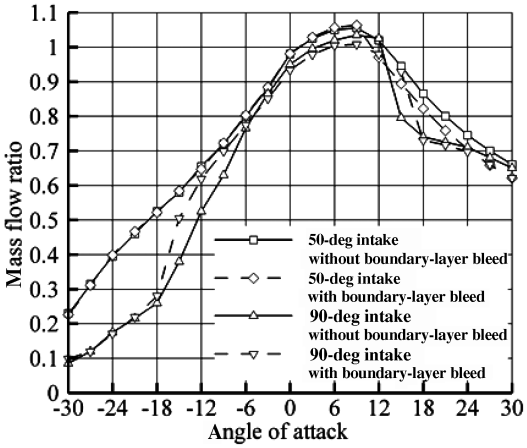

Fig. 11 Mass flow ratios of the 90-deg intake with and without boundary-layer bleed at $M_0 = 3.0$, α range.

Figure 12 shows the results, using Eq. (7), of all intakes with boundary-layer bleed. Again, the curve of the 70-deg intake is positioned between the curves of the other two chin intakes. Particularly conspicuous is a development almost identical to that in Fig. 9, with the exception that on the windward and leeward side sharp bends appear with a difference of about $\Delta\alpha = 3$ deg to larger angles. In a similar way, the expected additive mass flow loss can be clearly seen, compared with Figs. 9 and 12. At angles of attack $\alpha > 9$ deg, the mass flow ratios no longer overlap. It seems that the boundary-layer bleed reveals a different mode of operation, for example, the boundary-layer bleed of the 50-deg intake has an effect on angles of attack $\alpha > 9$ deg (Fig. 12).

The results of the tests with an angle of sideslip at $M_0 = 3.0$ have been mirrored because of the intakes' symmetry and are described briefly below. Figure 13 shows the normalized mass flow ratio without boundary-layer bleed in relation to the angle of sideslip between -30 deg $\leq \beta \leq 30$ deg. The influence of boundary-layer bleed is presented in Fig. 14. Here the performance curves of all three chin intakes show a pattern similar to the 360-deg intake. Compared

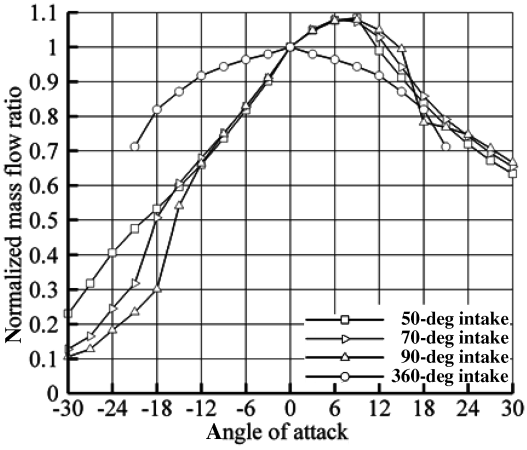

Fig. 12 Normalized mass flow ratios of all intakes at $M_0 = 3.0$, α range, with boundary-layer bleed.

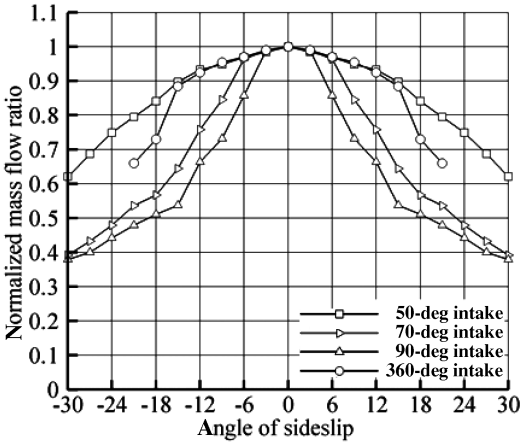

Fig. 13 Normalized mass flow ratios of all intakes at $M_0 = 3.0$, β range, without boundary-layer bleed.

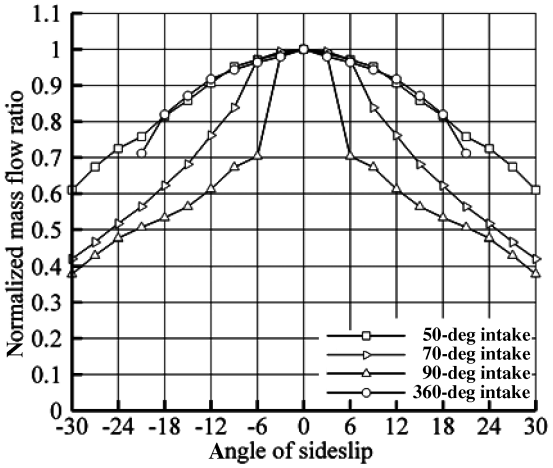

Fig. 14 Normalized mass flow ratios of all intakes at $M_0 = 3.0$, β range, with boundary-layer bleed.

with the variation in the angle of attack, the drop in the normalized mass flow ratio is sharper. It is more pronounced for the 90-deg intake and shows a clear decrease of the normalized mass flow ratio at sideslip angles beyond 6 deg. In general, the boundary-layer bleed does not yield improved performance in terms of normalized mass flow ratio.

To show the effect for the 90-deg intake more clearly, a comparison of the mass flow ratios $\dot{m}_3/\dot{m}_0$ for the cases with and without boundary-layer bleed is depicted in Fig. 15. It shows the slightly lower mass flow ratio at small angles of sideslip, and a stronger performance drop in the configuration with boundary-layer bleed is evident. When critically examined, the curves at angles of $\beta \geq \pm 15$ deg and at angles of $\alpha \geq -18$ deg (see Fig. 12) show that a failure of the boundary-layer bleed is possible. This means that, at large angles of sideslip, the pressure on the windward side is higher than on the opposite leeward side, that is, the air can pass through the drilled boundary-layer bleed holes (see Fig. 3) and can affect the intake's mass flow rate.

B. Flow Effects on the Windward and Leeward Sides

To achieve a better interpretation of the performance data, the flowfield around the model has been visualized by using the schlieren and oil flow techniques. Figure 16 shows an artist's impression of the model with its flow orientation, with a demonstration of the variation of the both angles, that is, the angles of attack and sideslip. For further explanation of flow phenomena, the tests in the α range (see Fig. 9) are chosen. In this range, the intake is clearly positioned on only one side (windward *or* leeward side) so that the flow effects can be

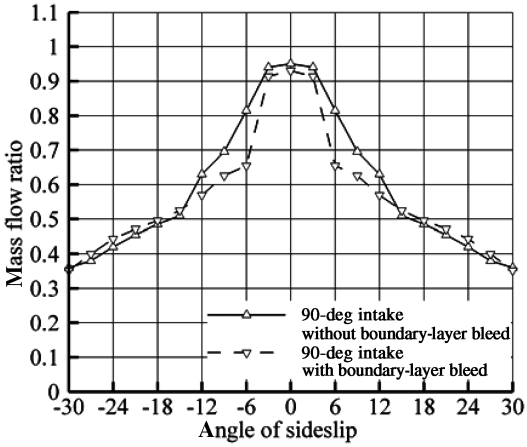

Fig. 15 Mass flow ratios of the 90-deg intake with and without boundary-layer bleed at $M_0 = 3.0$, β range.

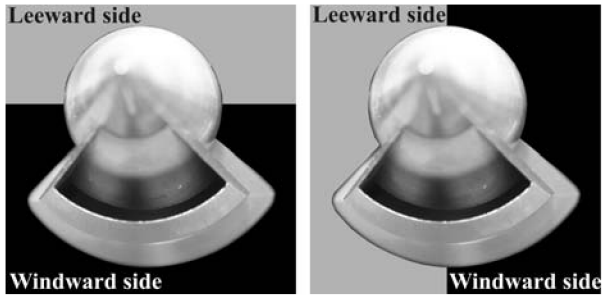

Fig. 16 Simplified illustration of the intake in the windward and leeward regions: a) $+\alpha$ range, and b) $+\beta$ range.

discussed separately. By comparison, in the β range the intake lies between the two regions so that both the windward and leeward flows affect the intake's performance.

As described in Fig. 7, an increase of the mass flow ratio over 1.0 is observed at positive angles of attack up to about $\alpha = 9$ deg. Figure 17 (exaggeratedly) is used to explain the reason for this increase. The effective intake area grows with the increasing angle of attack. Hence, the incident flow captured by the intake increases with the increasing positive angle of attack. Likewise, the shock angles decrease, so that the more acute-angled shocks are now at the intake lip and entering the intake. Pressure increases simultaneously on the windward side. The air is compressed downward in the effective intake area, with the effect that the operation at $\alpha > 0$ deg increases the external compression compared with the value at $\alpha = 0$ deg [19]. This results in a greater air density, thus causing higher compression with an increase in mass flow. Because these parameters are not considered in the determination of the reference mass flow rate $\dot{m}_0$, a mass flow ratio of greater than 1.0 can be achieved.

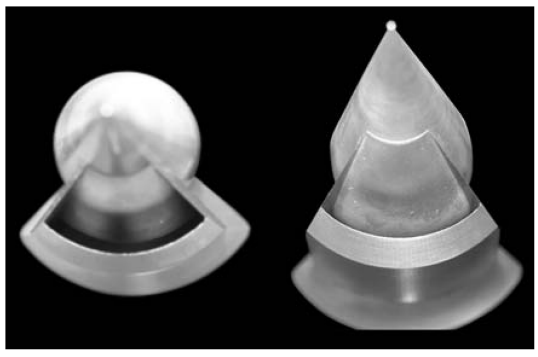

Fig. 17 Effective intake area of the 90-deg intake.

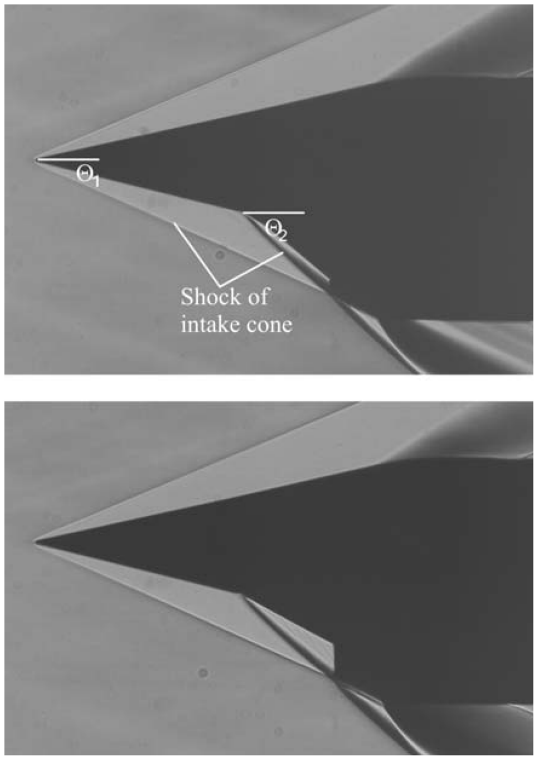

Fig. 18 Schlieren images at $\alpha = 0$ deg, $M_0 = 3.0$: a) 50-deg intake, and b) 90-deg intake.

Considering the schlieren images of the 50- and 90-deg intake at $\alpha = 0$ deg in Fig. 18, the similarity of the cone shocks is obvious. Looking at the cowl of the 90-deg intake, the shocks cause spillage; this was mentioned in Sec. III.A. Comparing the two shock angles of the schlieren images with the inviscid results of the design program [10], which are $\Theta_1 = 23.8$ deg and $\Theta_2 = 40.5$ deg (see also [20]), the difference between the measured and calculated values is ± 0.5 deg depending on the boundary layer and the quality of the schlieren images. The schlieren images show an averaged information of the actual three-dimensional flow including shocks, so that the sharpness of the shocks are influenced by the depth of the flow.

Another unexplained performance feature is linked to the next region with an angle of attack of $\alpha > 9$ deg, where a large mass flow loss is detected (Figs. 9 and 11). The schlieren images of the 50- and 90-deg intake are taken in a supercritical condition at $M_0 = 3.0$ (Fig. 19). They show the flow topology upstream of the intake at $\alpha = 9$, 12 deg ($\dot{m}_3/\dot{m}_0 > 1.0$) and at $\alpha = 15$ deg ($\dot{m}_3/\dot{m}_0 \approx 0.79$ of 90-deg intake).

Looking at the model at $\alpha = 9$ deg, the shocks are not well focused on the cowl. They are slightly under the cowl and closer to the main body and grow closer together with a growing angle of attack. Comparing the schlieren images of the 50-deg intake with the 90-deg intake, they have the same shock geometry, but the 90-deg intake has stronger shocks than the 50-deg intake, whereas with a growing angle, the intensity grows. Here, the cones' shocks intersect, which results in a slip line. Slip lines interfere with the intake's performance and can cause buzzing [21,22]. In the schlieren images at $\alpha = 12$ deg the normal shock appears right at the intake's entrance causing a slight mass flow loss. At an increasing angle of attack ($\alpha = 15$ deg), the normal shock is located on the second cone segment upstream. At this point, the shock system is responsible for spillage (see Fig. 11), especially in the case of the 90-deg intake, in which the shock system is stronger and broader than on the other intake. In this condition, the normal shock crosses the two cone

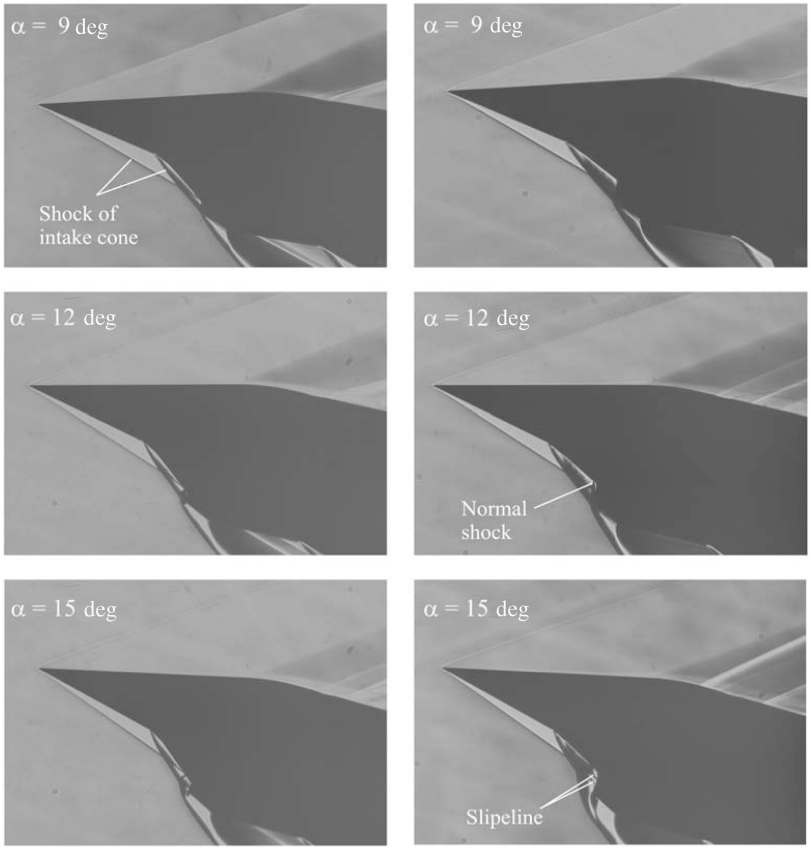

a) b)

Fig. 19 Schlieren images at $\alpha = 9$, 12, and 15 deg, $M_0 = 3.0$: a) 50-deg intake, and b) 90-deg intake.

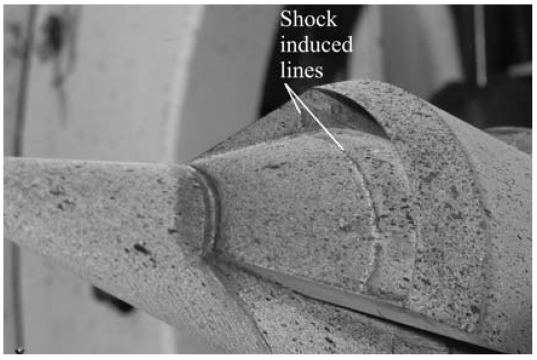

Fig. 20 Surface streamlines of 90-deg intake entrance at $\alpha = 15$ deg, $M_0 = 3.0$.

shocks and results in two slip lines entering the intake. These cause early buzzing and a short supercritical region in the characteristic diagram (Fig. 10).

Looking more closely at the intake's surface, Fig. 20 shows an oil flow image that was taken with the 90-deg intake at $\alpha = 15$ deg. The model is positioned to afford a better view of the surface streamlines. Right at the intake's entrance, color has been wiped off, so that a black line appears. It spans the cone segment and the segment wall. This induced line points to the normal shock, which confirms the occurrence in the schlieren images (Fig. 19).

Furthermore, on the leeward side at negative angles of attack the characteristics are different (Fig. 8). They have a constant mass flow loss, whereas the larger the intake's segment, the earlier the appearance is of the larger drop in the mass flow ratio (Figs. 9 and 12). At small angles, the mass flow losses appear because of the decrease in the external compression. With an increasing angle, the first cone masks the intake entrance and thus reduces mass flow. Leeward vortices then develop. The effect of the entering vortices is manifested by the sharp bends in Figs. 9, 11, and 12. With a further increase in the angle, the intensity of the vortices grows, and the vortices move closer to the center of the leeward side [8] so that the vortices with high-pressure losses enter the smaller chin intakes as well, which is demonstrated herein.

To gain a closer impression of the surface streamlines, the flowfield is visualized with the oil flow method. Figure 21 (top) demonstrates the streamlines of the leeward side. The surface

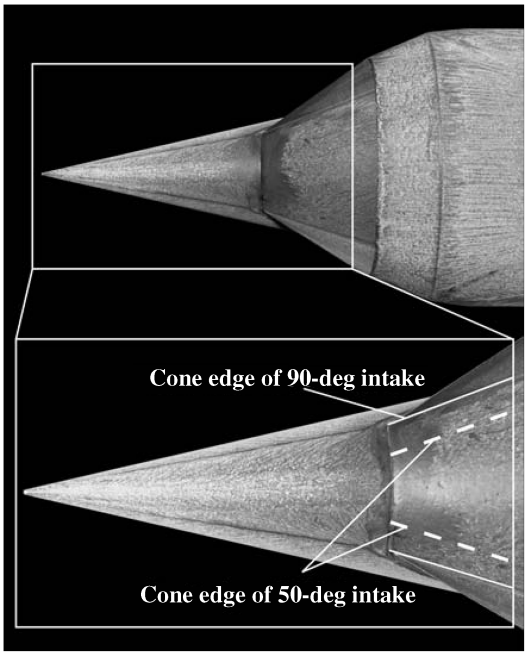

Fig. 21 Leeward surface streamlines of 90-deg intake at $\alpha = -18$ deg, $M_0 = 3.0$.

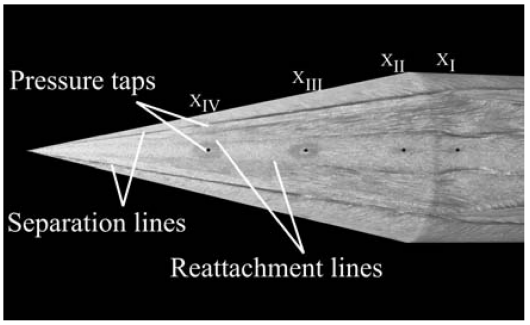

Fig. 22 Leeward surface streamlines of 26-deg cone model at $\alpha = -18$ deg, $M_0 = 3.0$.

streamlines are symmetrical and their pattern reveals counter-rotating vortices, which cause mass flow and pressure losses. The vortices develop from the apex of the cone, which means that the size and position of the intake's entrance are of great importance. With reference to Fig. 21 (bottom), the interpreted vortices on the first cone are completely entering the 90-deg intake, taking account of Herrmann and Triesch [8], where Pitot measurements show the development of vortices close to a 26-deg cone. In Fig. 21 (again, bottom), white dashed lines indicate the cone edge of the second cone segment of the 50-deg intake. Because the smaller entrance only collects a small part of the vortices, the influence on its performance is negligible (see Fig. 11).

Regarding the leeward surface streamlines, a conspicuous feature is the sharp black lines on the cone's surface, where the paint has been wiped off. The black lines seem to be an indication of embedded shocks [23] or of induced shocks from vortices. These kinds of shocks are also found in a similar investigation (see Seshadri and Narayan [24]).

A further investigation of the leeward side was performed with a 26-deg cone model. The model is equipped with 16 pressure taps (the black dots mark the pressure taps at $\varphi = 0$ deg in Fig. 22). Static pressure (Table 6) was detected at an angle of attack of $\alpha = -18$ deg, and afterwards the oil flow method was employed again. This time, the oil flow image in Fig. 22 displays a subtle distinction with, for example, separation and reattachment lines. The surface streamlines suggest a complex vortex system on the leeward side.

An examination of the pressure taps in Fig. 22 reveals limited resolution. Table 4 shows the results measured at the pressure taps on one half of the cone's leeward side (where X_I is at the shoulder and X_{IV} is close to the apex). Furthermore, the low pressure of the expansion at the shoulder is clearly visible. At $\varphi = 90$ deg, the flow circulates around the cone and so the static pressure is higher than on the leeward side, where the vortex systems develop.

IV. Conclusions

The performance of the three chin intakes with different entrance segments (90, 70, and 50 deg) has been studied in the Trisonic Wind Tunnel (TMK). These three intakes show differences in performance development during a maneuver flight at angles of attack (-30 deg $\leq \alpha \leq 30$ deg) and sideslip (-30 deg $\leq \beta \leq 30$ deg). The main reason for such differences is related to the complex flow phenomena around the missile.

Table 6 Static pressure of leeward side at $\alpha = -18$ deg, $M_0 = 3.0$

	Static pressure p_{st}, $\cdot 10^5$ Pa			
φ, deg	X_{IV}	X_{III}	X_{II}	X_I
90	——	0.273	0.266	——
45	0.129	0.128	0.126	0.048
0	0.161	0.161	0.163	0.071

Three main flow phenomena affecting the intake's performance have been identified. On the windward side, a higher external compression leads to an increase in mass flow between $\alpha = 0$ and 9 deg. For $\alpha \geq 12$ deg, a shock system in front of the intake's entrance causes spillage. At negative angles of attack, symmetrical vortices develop from the apex of the cone and affect the chin intake's performance, for example, the 90-deg intake with the largest intake entrance reacts most sensitively. For angles of sideslip, these effects appear together and affect the chin intake to different degrees. For example, these effects cause high losses in mass flow even at small angles of sideslip. This is comparable to the axially symmetrical intake tested before, where these effects intermix at all times. An improvement in the intake's performance is only achieved with the implementation of boundary-layer bleed at angles of attack. At angles of sideslip, the boundary-layer bleed is simply reflected in a mass flow loss because of its bleed.

This study shows the influence of the incident flow on the ramjet and its entrance. The flow effects such as shock systems or vortices can occur separately or together. These lead to losses, which not only affect the ramjet's performance but also the efficiency of combustion. The losses due to the vortices can be reduced, for example, with strakes [25], which are placed on the missile's nose to change the positions of the vortex systems. Another possibility is the use of air jets [26,27]. Two holes are therefore located at the very front. Through these holes, compressed air is blown out to displace the vortices away so that they do not affect the ramjet.

Acknowledgments

This study was carried out in the context of the DLR project, Missile of High Agility (HaFK). The authors gratefully acknowledge the support from the DLR Aeronautics and Energy Program Directorate.

References

[1] Seddon, J., and Goldsmith, E. L., *Intake Aerodynamics*, AIAA Education Series, AIAA, New York, 1985.

[2] Seddon, J., and Goldsmith, E. L., *Practical Intake Aerodynamic Design*, AIAA Education Series, AIAA, Washington, D.C., 1993.

[3] Colville, J. R., Starkey, R. P., and Lewis, M. J., "Extending the Flight Number of the SR-71 Inlet," AIAA Paper 2005-3284, 2005.

[4] Kojima, T., Sato, T., Sawai, S., and Tanatsugu, N., "Experimental Study on Restart Control of a Supersonic Air-Breathing Engine," *Journal of Propulsion and Power*, Vol. 20, No. 2, March–April 2004, pp. 273–279.

[5] Neale, M. C., and Lamb, P. J., *More Tests with a Variable Ramp Intake Having a Design Mach Number of 2.2*, Aeronautical Research Council, London, 1967.

[6] Hirschen, C., Herrmann, D., and Gülhan, A., "Experimental Investigation of the Performance and Unsteady Behavior of a Supersonic Intake," *Journal of Propulsion and Power*, Vol. 23, No. 3, May–June 2007, pp. 566–574. doi:10.2514/1.25103

[7] Harloff, G. J., and Smith, G. E., "Supersonic-Inlet Boundary-Layer Bleed Flow," *AIAA Journal*, Vol. 34, No. 4, April 1996, pp. 778–785.

[8] Herrmann, D., and Triesch, K., "Experimental Investigation of Isolated Inlets for High Agile Missiles," *Aerospace Science and Technology*, Vol. 10, No. 8, Dec. 2006, pp. 659–667. doi:10.1016/j.ast.2006.05.004

[9] Esch, H., "Die 0.6 m × 0.6 m—Trisonische Meßstrecke (TMK) der DFVLR in Köln-Porz," DFVLR-Mitt, 86-21, Köln, 1986.

[10] Anderson, B. H., "Design of Supersonic Inlets by a Computer Program Incorporating the Method of Characteristic," NASA TN-D-4960, 1968.

[11] Van Wie, D. M., "Scramjet Inlets," *Scramjet Propulsion*, edited by E. T. Curran, and S. N. B. Murthy, AIAA Progress in Astronautics and Aeronautics, AIAA, Reston, VA, 2000, pp. 447–511.

[12] "Durchflussmessung von Fluiden mit Drosselgeräten in voll durchströmten Leitungen mit Kreisquerschnitt—Teil 1: Allgemeine Grundlagen und Anforderungen," Deutsche Fassung EN ISO 5167-1:2003, DIN Deutsches Institut für Normung, e. V., Beuth Verlag GmbH, Berlin, Jan. 2004;also "Measurement of Fluid Flow by Means of Pressure Differential Devices Inserted in Circular Cross-Section Conduits Running Full—Part I: General Principles and Requirements," ISO 5167-1:2003.

[13] "Durchflussmessung von Fluiden mit Drosselgeräten in voll durchströmten Leitungen mit Kreisquerschnitt—Teil 2: Blenden," Deutsche Fassung EN ISO 5167-2:2003, DIN Deutsches Institut für Normung, e. V., Beuth Verlag GmbH, Berlin, Jan. 2004;also "Measurement of Fluid Flow by Means of Pressure Differential Devices Inserted in Circular Cross-Section Conduits Running Full—Part II: Orifice Plates," ISO 5167-2:2003

[14] Hünecke, K., *Flugtriebwerke—Ihre Technik und Funktion*, Motorbuch Verlag, Stuttgart, Germany, 1976.

[15] Oswatitsch, K., "Der Druckrückgewinn bei Geschossen mit Rückstoßantrieb bei hohen Überschallgeschwindigkeiten," Deutsche Versuchsanstalt für Luftfahrt, e. V., Bericht Nr. 49, Dec. 1957.

[16] Goldsmith, E. L., and Seddon, J., *Practical Intake Aerodynamic Design*, AIAA Education Series, AIAA, New York, 1993, pp. 1–20.

[17] Krohn, E.-O., "Inlet Buzz in Ramjets and its Suppression," *AIAA Eighth International Symposium on Air Breathing Engines*, AIAA, New York, 1987, pp. 110–117;also AIAA Paper 87-7006

[18] Settles, G. S., *Schlieren and Shadowgraph Techniques—Visualizing Phenomena in Transparent Media*, Springer–Verlag, Berlin/Heidelberg, 2001.

[19] Mahoney, J. J., *Inlet for Supersonic Missiles*, AIAA Education Series, AIAA, Washington, D.C., 1990.

[20] Ames Research Staff, "Equations, Tables, and Charts for Compressible Flow," National Advisory Committee for Aeronautics Rept. 1135, Langley Field, VA, 1953, pp. 613–681.

[21] Jungclaus, G., "Neue experimentelle Ergebnisse zur Entstehung und Struktur von Ferri- und Dailey-Instabilitäten ("Brummen")," *Zeitschrift für Flugwissenschaften und Weltraumforschung*, Springer–Verlag, Vol. 14, 1990, pp. 256–262.

[22] Krohn, E.-O., and Triesch, K., "Untersuchungen zur Ferri-Instabilität bei Überschalleinläufen," DFVLR-Forschungsbericht 85-53, Köln, Germany, 1985.

[23] Boersen, S. J., "Reynolds Number Effects on Pressure and Normal Force Distributions Along Conically Pointed Circular Cylinder at Free-Stream Mach Number of 2.3," National Aerospace Laboratory TR 75124 U, Netherlands, 1975.

[24] Seshadri, S. N., and Narayan, K. Y., "Possible Types of Flow on Lee-Surface of Delta Wings at Supersonic Speeds," *Aeronautical Journal*, Paper 1543, May 1988. pp. 185–199.

[25] Malcolm, G. N., "Forebody Vortex Control—A Progress Review," AIAA Paper 93-3540-CP, 1993.

[26] Skow, A. M., and Peake, D. J., *Control of the Forebody Vortex Orientation by Asymmetric Air Injection: (Part A) Application to Enhance Departure/Spin Recovery of Fighter Aircraft and (Part B) Details of the Flow Structure*, AGARD Lecture Series, No. 121, 1982, pp. 10-1–10-22.

[27] Roos, F. W., "Microblowing for High-Angle-of-Attack Vortex Flow Control on a Fighter Aircraft," *Journal of Aircraft*, Vol. 38, No. 3, May–June 2001, pp. 454–457.

[28] Kantrowitz, A., and Donaldson, C. duP., "Preliminary Investigation of Supersonic Diffusers," Wartime Report, NACA WR L-713, Washington, D.C., 1945.

F. Liu
Associate Editor